Chinese Chemical Letters 37 (2026) 111558

Contents lists available at ScienceDirect

Chinese Chemical Letters

journal homepage: www.elsevier.com/locate/cclet

Boosting ionic conductivity in $Li_xAlCl_{3-x}O_x$ solid electrolytes through anion-mixing-engineered ion diffusion channels

Liming Zhang[a,1], Chenjie Lou[b,1], Shuaika Liang[c,1], Wei Xia[c], Rui Wang[d], Longfei Li[a], Chengyu Fu[a], Mingxue Tang[b], Rong Xiang[e], Wei Wang[f], Yichun Xu[g,*], Hongfa Xiang[a,*], Xuyong Feng[a,*]

[a] School of Materials Science and Engineering, Anhui Provincial Key Laboratory of Advanced Functional Materials and Devices, Hefei University of Technology, Hefei 230009, China
[b] Center for High Pressure Science and Technology Advanced Research, Beijing 100193, China
[c] Ningbo Key Laboratory of All-Solid-State Battery, Eastern Institute for Advanced Study, Eastern Institute of Technology, Ningbo 315201, China
[d] Faculty of Materials Science and Chemistry, China University of Geosciences, Wuhan 430074, China
[e] State Key Laboratory of Fluid Power and Mechatronic Systems, Zhejiang Provincial Key Laboratory for Atomic-level Manufacturing, School of Mechanical Engineering, Zhejiang University, Hangzhou 310027, China
[f] CAS Key Laboratory of Design and Assembly of Functional Nanostructures, Fuzhou 360002, China
[g] Institute of Solid State Physics, Hefei Institutes of Physical Science, Chinese Academy of Sciences, Hefei 230031, China

ARTICLE INFO

Article history:
Received 28 May 2025
Revised 4 July 2025
Accepted 8 July 2025
Available online 8 July 2025

Keywords:
All solid-state batteries
Mix anion solid state electrolytes
Halide
Solid state NMR
Neutron pair distribution function

ABSTRACT

Solid-state electrolytes composed of earth-abundant elements offer significant cost advantages for large-scale energy storage applications. However, their widespread adoption is hindered by inherently low ionic conductivity. In this study, we report a low-cost solid-state electrolyte, $Li_xAlCl_{3-x}O_x$ ($0.6 \leq x \leq 1.1$), with dramatically enhanced ionic conductivity achieved through the construction of fast ion-conducting channels *via* an innovative anion mixing strategy. First-principles calculations and experimental characterizations reveal that the Cl^-/O^{2-} anion mixing expands the distribution of Li^+ ions within the lattice while reducing the distance between adjacent sites. This structural optimization results in a low Li^+ migration activation energy of 0.3 eV and elevates the ionic conductivity from 10^{-3} mS/cm to 1.5 mS/cm. Furthermore, the Cl^-/O^{2-} mixing synergistically combines the advantages of both anions, endowing the $Li_xAlCl_{3-x}O_x$ electrolyte with high-voltage stability (up to 3.96 V *vs.* Li^+/Li), robust interfacial compatibility, and air stability. When integrated into all-solid-state batteries with a $LiCoO_2||Li_{0.8}AlCl_{2.2}O_{0.8}||Li_6PS_5Cl||Li$-Si configuration, it delivers an initial capacity of 127 mAh/g and retains 94.4% of its discharge capacity after 180 cycles at 0.3 C.

© 2026 Published by Elsevier B.V. on behalf of Chinese Chemical Society and Institute of Materia Medica, Chinese Academy of Medical Sciences.

The high cost of solid-state electrolytes (SSEs) poses a significant barrier to the industrial adoption of all-solid-state lithium-ion batteries (ASSLBs). This cost is primarily driven by two factors: the use of expensive raw materials and energy-intensive synthesis processes [1]. For instance, elements such as La in $Li_7La_3Zr_2O_{12}$ [2–6], Ge in $Li_{10}GeP_2S_{12}$ [7–9], and Sc/In Li_3ScCl_6/Li_3InCl_6 [10–12] are scarce and significantly increase material costs. Although earth-abundant elements like P, S, and Cl are used in sulfide SSEs (*e.g.*, Li_6PS_5Cl), the complex preparation process of Li_2S still elevates the overall cost [13]. Similarly, oxide electrolytes with garnet and NASICON structures require sintering temperatures exceeding 1000 °C, leading to high energy consumption [4,14–17]. Halide SSEs, such as Li_2ZrCl_6, often involve inefficient synthesis methods like long time high-energy ball milling (500 rpm for 45 h) [18–23]. These challenges underscore the urgent need to develop low-cost SSEs composed of earth-abundant elements and scalable synthesis methods.

Aluminum (Al), the most abundant metallic element in the Earth's crust (Figs. S1a and b in Supporting information), offers a promising solution. Aluminum chloride ($AlCl_3$), a low-cost precursor with a melting point of 194 °C, enables the synthesis of SSEs (*e.g.*, $LiAlCl_4$) at relatively low temperatures (<200 °C) [24–27]. However, the ionic conductivity of solid $LiAlCl_4$ remains low (10^{-6} S/cm at 25 °C), limiting its applicability in ASSBs [24,28].

The ionic conductivity of SSEs is closely tied to their structural properties. Short distances between adjacent charge carriers, par-

* Corresponding authors.
E-mail addresses: xuyichun@issp.ac.cn (Y. Xu), hfxiang@hfut.edu.cn (H. Xiang), 2021800026@hfut.edu.cn (X. Feng).
[1] These authors contributed equally to this work.

https://doi.org/10.1016/j.cclet.2025.111558
1001-8417/© 2026 Published by Elsevier B.V. on behalf of Chinese Chemical Society and Institute of Materia Medica, Chinese Academy of Medical Sciences.

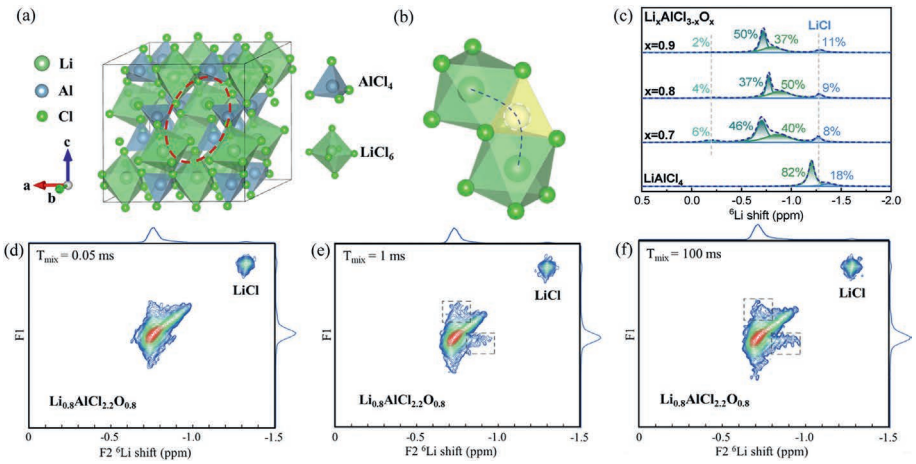


Fig. 1. (a) The structural model of $LiAlCl_4$. The light green, light blue, and green balls represent Li, Al, and Cl atoms, respectively. (b) Li^+ ion diffusion path between adjacent octahedral sites. (c) Solid-state ^6Li NMR spectra of $Li_xAlCl_{3-x}O_x$. (d-f) 2D exchange NMR spectra of $Li_{0.8}AlCl_{2.2}O_{0.8}$ with different mixing times.

ticularly in face-sharing polyhedra, are critical for achieving rapid ion conduction. Notable examples include body-centered sulfides [29–33] and $LaCl_3$-based Li^+/Na^+ conductors [34,35]. In $LiAlCl_4$, however, all Li^+ ions occupy octahedral sites (4e, O site), which are either corner-sharing or edge-sharing, with a Li-Li distance exceeding 4.22 Å (Fig. 1a). The migration of Li^+ ions between adjacent octahedral sites involves passing through one or two tetrahedral sites (T site), following an O-T-O or O-T-T-O pathway. The higher site energy of tetrahedral sites increases the activation energy for ion diffusion, resulting in low ionic conductivity (Fig. 1b and Fig. S2 in Supporting information) [25]. Previous studies have shown that structural distortion induced by high-energy ball milling can reduce the energy of Li^+ ions in tetrahedral sites, enabling partial relocation of Li^+ ions to these sites [24]. This approach increases the ionic conductivity of $LiAlCl_4$ by approximately 20 times, reaching 2.1×10^{-5} S/cm [24]. Nevertheless, this value remains insufficient for practical applications.

Anion mixing has emerged as an effective strategy for tuning the site energy and distribution of Li^+ ions in SSEs. Since anions directly coordinate with Li^+ ions, they exert a strong influence on Li^+ site energy. Anion mixing (*e.g.*, Cl^-/O^{2-}, S^{2-}/Cl^-, and S^{2-}/O^{2-}) enables Li^+ ions to occupy a wider range of sites, shortening the migration distance between charge carriers and enhancing ionic conductivity [18,36–45]. In this study, we employ Cl^-/O^{2-} mixing to significantly improve the ionic conductivity of $Li_xAlCl_{3-x}O_x$. This strategy increases the number of Li^+-occupied sites and reduces the distance between adjacent sites, leading to a lower ion migration activation energy (0.30 eV) and a remarkable enhancement in ionic conductivity (1.5×10^{-3} S/cm).

The electrolyte developed in this study uses $AlCl_3$ and LiOH as raw materials and can be prepared with heating at 200 °C for only 0.5 h (Fig. S1c in Supporting information). In contrast to crystalline $LiAlCl_4$, the synthesized $Li_xAlCl_{3-x}O_x$ exhibits a pure amorphous structure (Fig. S3 in Supporting information). The incorporation of O^{2-} into $Li_xAlCl_{3-x}O_x$ likely facilitates the formation of highly stable Al−O−Al fragments. During cooling from the molten state, the presence of these Al−O−Al fragments restricts atomic rearrangement (crystallization), resulting in the retention of an amorphous structure at room temperature [43]. However, when x exceeds 0.8, a LiCl phase emerges in the product, and its content increases with higher O^{2-} concentrations (Fig. S3). This is because the enthalpy (H) and entropy (S) of $Li_xAlCl_{3-x}O_x$ increases upon the incorporation of O^{2-} (Li^+) and formation of defects (O^{2-} substituted Cl^-, interstitial Li^+). When $\Delta G = \Delta H - T\Delta S < 0$, the structure of $Li_xAlCl_{3-x}O_x$ would be thermal-dynamically stable ($x \leq 0.8$). Otherwise, the structure would be unstable and ultimately decompose to impurities such as LiCl ($x > 0.8$). In the main glass phase, more anion vacancies and fewer Li^+ interstitial defects would be formed ($Li_{x-y}AlCl_{3-x-y}O_x$). This indicates that the high energy of interstitial Li^+ ions is the main defect leading to instability of $Li_xAlCl_{3-x}O_x$.

The Cl^-/O^{2-} mixing in the amorphous phase is further confirmed by X-ray photoelectron spectroscopy (XPS) (Fig. S4 in Supporting information). The Li 1s and Al 2p spectral peaks for $Li_{0.8}AlCl_{2.2}O_{0.8}$ are situated between those of $LiAlCl_4$ and $LiAlO_2$, providing clear evidence of Cl^-/O^{2-} anion mixing in $Li_{0.8}AlCl_{2.2}O_{0.8}$.

Solid-state nuclear magnetic resonance (ssNMR) spectroscopy is a powerful tool for probing the local structure and distribution of Li^+ ions [46–48], providing critical insights into ion conduction mechanisms in $LiAlCl_4$ and $Li_xAlCl_{3-x}O_x$ (Figs. 1c-f). In $LiAlCl_4$, a single ^7Li resonance signal is observed, confirming that Li^+ ions exclusively occupy octahedral sites (4e sites) coordinated by six Cl^- ions (Fig. 1a and Fig. S5 in Supporting information) [43]. The introduction of O^{2-} significantly alters the local Li^+ environment in the halide SSE. The ^6Li NMR spectra of $Li_xAlCl_{3-x}O_x$ reveal three distinct resonance signals: one corresponding to the LiCl impurity (~−1.2 ppm) and two others (~−0.88 and −0.65 ppm) arising from different Li^+ sites within the $Li_xAlCl_{3-x}O_x$ structure (Fig. 1c). The presence of cross-peaks in the 2D exchange spectroscopy (EXSY) NMR spectra further confirms the rapid exchange of Li^+ ions between these two distinct sites (Figs. 1d-f). In the 1D spectra, all signals representing different Li^+ environments are clearly resolved. At a short mixing time (0.05 ms), the exchange of Li^+ ions between the two sites is negligible (Fig. 1d). However, as the mixing time is extended to 1 ms and 100 ms, distinct cross-peaks emerge between the two Li^+ chemical environments (−0.88 and −0.65 ppm), as highlighted in the dotted boxes in Figs. 1e and f. This observation demonstrates that Li^+ ions dynamically migrate between neighboring sites, creating efficient conduction pathways.

The incorporation of O^{2-} into $Li_xAlCl_{3-x}O_x$ significantly enhances its ionic conductivity, reaching values on the order of 10^{-3} S/cm at 25 °C. The composition is optimal at $x = 0.8$, when it is phase-pure amorphous without significant impurities (based on XRD), and the ionic conductivity reaches an optimum of 1.5×10^{-3} S/cm (Figs. 2a and c). For $x < 0.8$, the improvement in ionic conduction with increasing O^{2-} content is attributed to the rising defect density resulting from O^{2-}/Cl^- mixing. Conversely, for $x > 0.8$, the decline in ionic conductivity is due to the formation of impurities (Fig. S3). Additionally, the amorphous structure induced by O^{2-} doping should also facilitates the distribution of Li^+ ions

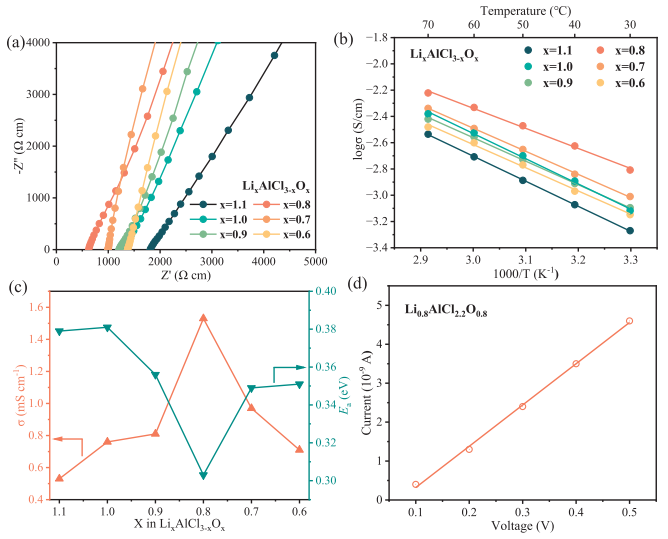


Fig. 2. (a) Nyquist plots, (b) Arrhenius plots, and (c) ionic conductivities and activation energies of $Li_xAlCl_{3-x}O_x$. (d) Electronic conductivity of $Li_{0.8}AlCl_{2.2}O_{0.8}$.

across multiple sites, further contributing to the enhanced ionic conductivity [24].

Conductivity measurements also reveal a significant reduction in activation energy to 0.30 eV for $Li_{0.8}AlCl_{2.2}O_{0.8}$ (Figs. 2b and c, Fig. S6 in Supporting information). Furthermore, the electronic conductivity of $Li_{0.8}AlCl_{2.2}O_{0.8}$, determined from DC polarization curves (Fig. 2d and Fig. S7 in Supporting information), is calculated to be 6.98×10^{-10} S/cm. This value is substantially lower than that of many widely studied solid-state electrolytes, highlighting the material's potential for minimizing electronic leakage in solid-state battery applications [49–51].

To elucidate the local structure of amorphous $Li_xAlCl_{3-x}O_x$ and gain deeper insights into Li^+ ion conduction pathways, density functional theory (DFT) calculations were performed (Figs. 3a-d). The initial structure of $Li_{0.75}AlCl_{2.25}O_{0.75}$ was constructed by replacing 0.75 Cl^- with O^{2-} in $AlCl_3$ and adding 0.75 Li^+ ions to maintain charge neutrality. The hypothesized structure was heated to 800 K for 10 ps with a time step of 1 fs to obtain a fully melted configuration. Subsequently, the amorphous structure was annealed at lower temperatures by adjusting the model size to achieve the appropriate pressure. The final structure of $Li_{0.75}AlCl_{2.25}O_{0.75}$ was energy-minimized (Fig. 3a and Table S1 in Supporting information). The simulated structure reveals that Al^{3+} ions remain in tetrahedral sites, with partial replacement of Cl^- by O^{2-} leading to the formation of Al-O-Al fragments (Fig. 3a and Fig. S8 in Supporting information). The framework of $Li_{0.75}AlCl_{2.25}O_{0.75}$ consists of $AlCl_nO_{4-n}$ units, while Li^+ ions occupy various interstitial sites, coordinated by different combinations of Cl^- and O^{2-} ions (*e.g.*, 3Cl, 1O2Cl, 4Cl, 2O3Cl). Compared to $LiAlCl_4$, the coordination environments of Li^+ ions in $Li_{0.75}AlCl_{2.25}O_{0.75}$ are more complex, resulting in two broad peaks in the NMR spectra (Fig. 2b). The substitution of Cl^- with the more electronegative O^{2-} reduces the electron cloud density around the Li^+ nucleus, leading to a larger chemical shift (toward the left) [36,52]. Consequently, the left-shifted ^6Li peak (−0.65 ppm) likely corresponds to Li^+ ions coordinated with a higher number of O^{2-} anions.

Compared to $LiAlCl_4$, where Li^+ ions predominantly occupy octahedral sites, the increased distribution of Li^+ sites in $Li_xAlCl_{3-x}O_x$ suggests a reduction in the distance between adjacent Li^+ sites. A segment of the simulated $Li_{0.75}AlCl_{2.25}O_{0.75}$ structure (Fig. 3b) confirms that the Li–Li distance (3.03–3.80 Å) is significantly shorter than that in $LiAlCl_4$ (4.22–4.88 Å). This observation is further supported by the radial distribution function (RDF) of Li–Li (Fig. 3c),

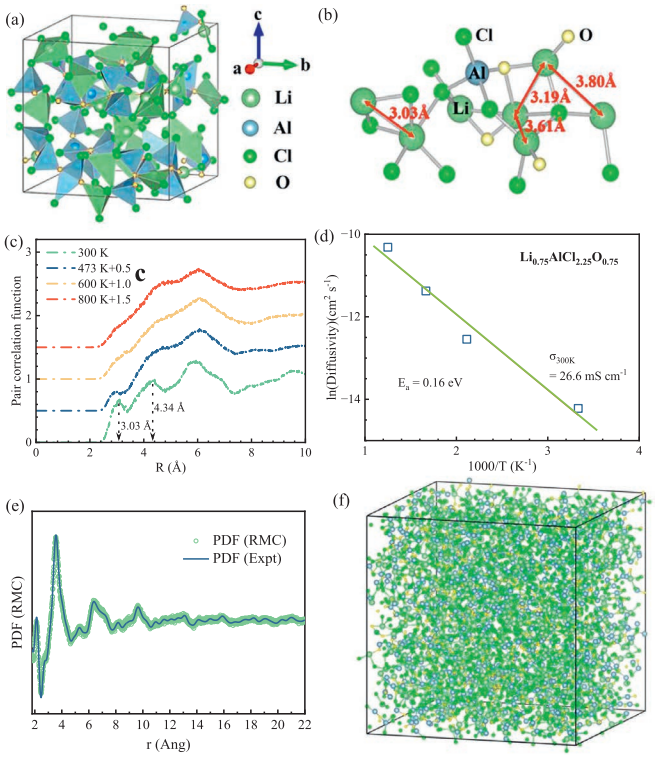


Fig. 3. (a) Simulated structure of $Li_{0.75}AlCl_{2.25}O_{0.75}$. (b) Microstructural fragments of $Li_{0.75}AlCl_{2.25}O_{0.75}$ with the shortest Li^+ transition distances. (c) The RDF of Li–Li in $Li_{0.75}AlCl_{2.25}O_{0.75}$ at different temperatures. R represents the distance between different Li^+ ions. (d) The Arrhenius plots of Li-ion diffusivity as a function of temperature for $Li_{0.75}AlCl_{2.25}O_{0.75}$. (e) Neutron pair distribution function (nPDF) analysis of $Li_{0.8}AlCl_{2.2}O_{0.8}$ from total neutron scattering data. (f) Expanded structure ($3 \times 3 \times 3$) of $Li_{0.75}AlCl_{2.25}O_{0.75}$ after refinement with nPDF results.

which reveals shorter Li-Li distances in $Li_{0.75}AlCl_{2.25}O_{0.75}$. Additionally, the peaks corresponding to short Li-Li distances gradually diminish with increasing temperature, indicating structural collapse at elevated temperatures. At 600 K, the loss of short-range order confirms that $Li_{0.75}AlCl_{2.25}O_{0.75}$ transitions to a molten state.

In solid-state electrolytes (SSEs), the distribution of Li^+ ions is governed by their site energy at different interstitial positions, which is primarily determined by the bond energy between Li^+ ions and surrounding anions. This bond energy can be described by the equation $E(r) = -\frac{Z_i Z_j}{4\pi\varepsilon_0 r} + \frac{B}{r^n}$, where ε_0 is the dielectric constant, B and n are constant, Z_i and Z_j are ion charge number, r is the distance between Li^+ ions and surrounding anions [44]. When the anion type changes, the site energy and Li^+ distribution in SSEs undergo significant modifications. In chloride-based SSEs, Li^+ ions predominantly occupy octahedral interstices, where the distance between adjacent sites is relatively large. However, upon the introduction of O^{2-} ions, the site energy of Li^+ in tetrahedral and interstitial sites decreases, increasing the number of favorable distribution sites. Consequently, the distance between adjacent Li^+ sites is substantially reduced.

The Li^+ ion conduction in $Li_{0.75}AlCl_{2.25}O_{0.75}$ was also simulated (Fig. 3d). The Li^+ diffusion coefficients range from 10^{-6} cm^2/s to 10^{-5} cm^2/s between 300 K and 800 K, demonstrating rapid ion migration across this temperature range [38]. The calculated activation energy (0.16 eV) and ionic conductivity (26.6 mS/cm at 300 K) further confirm the presence of fast ion-diffusion channels and efficient ion conduction in $Li_{0.75}AlCl_{2.25}O_{0.75}$. Notably, the Li^+ ion probability densities reveal potential diffusion pathways (Fig. S9 in Supporting information). At 300 K, Li^+ ions exhibit partial long-range diffusion through low-energy pathways. As the temperature

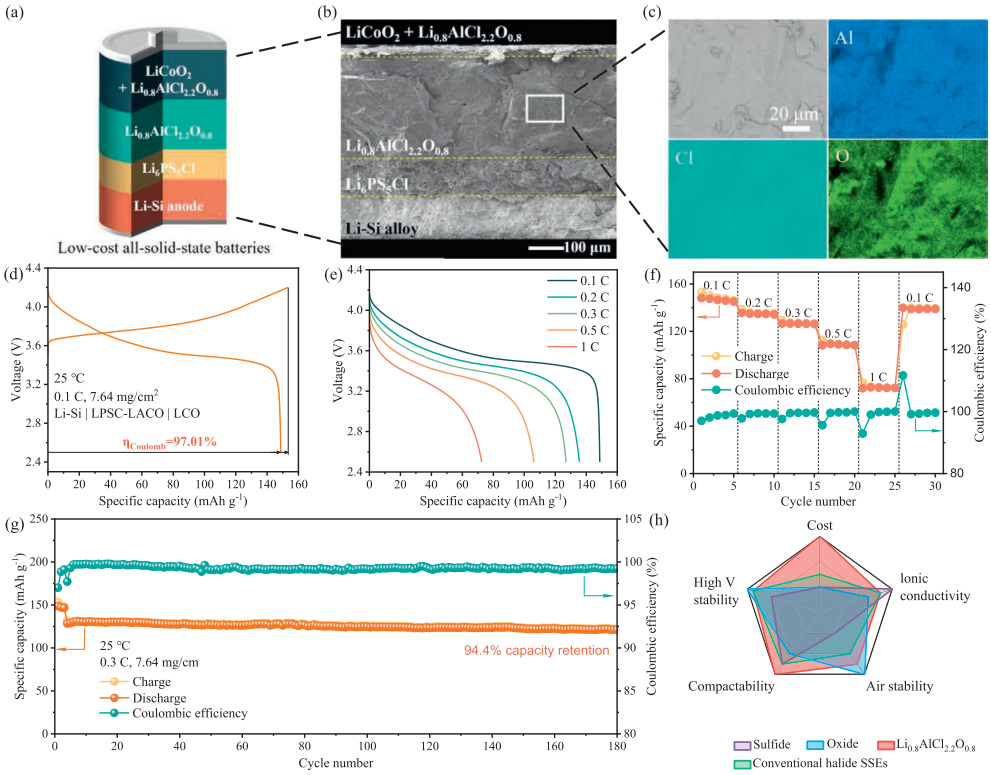


Fig. 4. Electrochemical performance of the $LiCoO_2$||$Li_{0.8}AlCl_{2.2}O_{0.8}$||$Li_6PS_5Cl$||Li-Si cell. (a) Schematic illustration of the ASSBs. (b) SEM image of cross-sectional ASSBs. (c) EDS image of $Li_{0.8}AlCl_{2.2}O_{0.8}$. (d) The initial charge/discharge curves at 0.1 C, with the Coulombic efficiency $\eta_{Coulomb}$ denoted. (e) Discharge profiles at different current densities. (f) Rate capability at 0.1, 0.2, 0.3, 0.5 and 1 C. (g) Long-term cycling performance at 0.3 C. (h) Spider plot comparing the performance of sulfide, oxide, conventional halide SSEs and $Li_{0.8}AlCl_{2.2}O_{0.8}$ [58–66].

increases to 600 K and 800 K, the more uniform probability densities suggest a flatter energy landscape in $Li_{0.75}AlCl_{2.25}O_{0.75}$.

The simulated structure was further validated by neutron pair distribution function (nPDF) analysis. The PDF profile features a peak at 2.165 Å, corresponding to Al-Cl pairs, while strong peaks at 3.595 Å and 6.425 Å are attributed to Al-Al pairs. Below 6 Å, $Li_{0.8}AlCl_{2.2}O_{0.8}$ exhibits multiple strong peaks, indicative of its characteristic short-range order. Beyond 10 Å, the peak intensity diminishes, reflecting the material's long-range disorder and amorphous nature, consistent with XRD results. To improve refinement accuracy, the structural unit of $Li_{0.75}AlCl_{2.25}O_{0.75}$ was expanded to a $3 \times 3 \times 3$ supercell. The refined nPDF spectrum yields an good fit ($\chi^2 = 4.8$), validating the simulated $3 \times 3 \times 3$ structure (Fig. 3e) [53]. The refined structure is shown in Fig. 3f, which closely matches the initial simulation.

Like other chloride solid electrolytes, $Li_{0.8}AlCl_{2.2}O_{0.8}$ is susceptible to deliquescence in natural air [54], but the electrolyte is well stabilized in dry air. After exposing $Li_{0.8}AlCl_{2.2}O_{0.8}$ to a dry room atmosphere (dew point: −40 °C) for 24 h, the ionic conductivity decreased slightly from 1.5 mS/cm to 1.1 mS/cm, while the amorphous structure remained intact (Fig. S10 in Supporting information). A minor mass increase from 0.3346 g to 0.3449 g further confirms its stability in dry air, attributed to the strong Al-O and Li-O bonds. Linear sweep voltammetry (LSV) of $Li_{0.8}AlCl_{2.2}O_{0.8}$-Super P||$Li_{0.8}AlCl_{2.2}O_{0.8}$||Li reveals an electrochemical stability window ranging from 1.12 V to 3.96 V *vs.* Li^+/Li (Fig. S11 in Supporting information), comparable to other halide solid-state electrolytes [34,55].

To assess the practical applicability of $Li_{0.8}AlCl_{2.2}O_{0.8}$ as a solid-state electrolyte (SSE), an all-solid-state battery (ASSB) was assembled using a commercial $LiCoO_2$ composite cathode and a homemade Li-Si anode. A transition layer of homemade Li_6PS_5Cl was incorporated to isolate the $Li_{0.8}AlCl_{2.2}O_{0.8}$ SSE from the Li-Si anode (Fig. 4a). Given the electrochemical stability window of $Li_{0.8}AlCl_{2.2}O_{0.8}$, it was employed as a catholyte in the composite cathode. To enhance stability, Li-Si (with a higher potential than Li metal) was selected as the anode [56], while Li_6PS_5Cl (Fig. S12 in Supporting information), known for its compatibility with anodes, was used as the anolyte to separate $Li_{0.8}AlCl_{2.2}O_{0.8}$ from the Li-Si anode. To minimize oxidation and decomposition of $Li_{0.8}AlCl_{2.2}O_{0.8}$ above its oxidation potential (3.96 V *vs.* Li^+/Li), conductive carbon was excluded from the composite cathode, enabling $LiCoO_2$ to be charged to 4.2 V *vs.* Li-Si [57].

Cross-sectional SEM images of the ASSB (Figs. 4b and c) reveal layer thicknesses of ~24 μm ($LiCoO_2$ composite cathode), 300 μm ($Li_{0.8}AlCl_{2.2}O_{0.8}$ SSE), 110 μm (Li_6PS_5Cl SSE), and 130 μm (Li-Si anode). High-magnification SEM images (Fig. S13 in Supporting information) confirm the dense morphology of the $Li_{0.8}AlCl_{2.2}O_{0.8}$ layer. Under a pressure of 150 MPa, $Li_{0.8}AlCl_{2.2}O_{0.8}$ appears compact and pinhole-free (Fig. S13b), while Li_6PS_5Cl exhibits a porous structure (Fig. S13c). The total resistance of the ASSB before cycling exceeds 400 Ω (Fig. S14 in Supporting information), primarily attributed to the composite cathode (Fig. S15 in Supporting information). This high resistance stems from the high content (75 wt%) of poorly conductive $LiCoO_2$ in the cathode layer.

The $LiCoO_2$||$Li_{0.8}AlCl_{2.2}O_{0.8}$||$Li_6PS_5Cl$||Li-Si ASSB was cycled at various current densities between 2.5 V and 4.2 V under an operating pressure of 120 MPa at 25 °C (Figs. 4d-g). At 0.1 C (25 °C), the battery delivers a discharge capacity of 150 mAh/g with a high initial Coulombic efficiency (CE) of 97 %, indicating highly reversible reactions (Fig. 4d). This performance underscores the effectiveness of the battery configuration and the excellent oxidation stability of $Li_{0.8}AlCl_{2.2}O_{0.8}$, which minimizes side reactions during cycling. As the current density increases, the discharge capacities decrease to

138 mAh/g (0.2 C), 128 mAh/g (0.3 C), 108 mAh/g (0.5 C), and 73 mAh/g (1 C). The rate capability is currently limited by the high cathode resistance, necessitating further optimization of the cathode composition [67]. Remarkably, the ASSB retains 94.4% of its discharge capacity after 180 cycles at 0.3 C (Fig. 4g). Even after 1000 cycles at 1 C, the capacity retention reaches 70.6% (Fig. S16 in Supporting information), demonstrating exceptional cycling stability. Post-cycling resistance measurements (Fig. S14) reveal a slight reduction in total resistance after 180 cycles at 0.3 C or 1000 cycles at 1 C, further confirming the outstanding oxidation stability of $Li_{0.8}AlCl_{2.2}O_{0.8}$ SSE.

In conclusion, we have developed a low-cost $Li_xAlCl_{3-x}O_x$ solid-state electrolyte (SSE) through an innovative anion mixing strategy, which offers a compelling combination of low cost, high oxidation stability, excellent interfacial compatibility, and superior ionic conductivity (Fig. 4h). The use of earth-abundant elements significantly reduces material costs, while the short sintering time (30 min) at a low temperature (200 °C) further minimizes production expenses. The O^{2-}/Cl^- dual-anion design enables Li^+ ions to occupy multiple sites within the $Li_xAlCl_{3-x}O_x$ lattice, reducing Li^+ migration distances and enhancing ionic conductivity. The optimized $Li_xAlCl_{3-x}O_x$ SSE achieves a room-temperature ionic conductivity of 1.5 mS/cm, representing a three-order-of-magnitude improvement over $LiAlCl_4$. The incorporation of O^{2-} into the $AlCl_3$-based halide not only improves oxidation stability but also enhances air stability, owing to the stronger bonding between O^{2-} and Li^+/Al^{3+}. The dense morphology of $Li_xAlCl_{3-x}O_x$ SSE ensures excellent interfacial contact with the cathode, further supporting its practical application. The exceptional oxidation stability and compactability of $Li_xAlCl_{3-x}O_x$ make it a promising catholyte candidate for all-solid-state batteries (ASSBs). In a proof-of-concept demonstration, a $LiCoO_2$/Li-Si ASSB incorporating $Li_{0.8}AlCl_{2.2}O_{0.8}$ as the catholyte delivered outstanding electrochemical performance, achieving a high initial Coulombic efficiency of 97% and retaining 94.4% of its discharge capacity after 180 cycles at 0.3 C. These results highlight the significant potential of $Li_xAlCl_{3-x}O_x$ SSEs for practical applications in next-generation solid-state batteries. However, the absence of conductive carbon and the high weight ratio of low conductive $LiCoO_2$ (75%) at the cathode make the ASSB have high resistance which affects the rate performance. Further research could be enhancement of oxidation stability of SSE, adding conductive carbon if stability allows, or surface modify the $LiCoO_2$ cathode to improve the battery performance.

CRediT authorship contribution statement

Liming Zhang: Writing – original draft, Methodology, Formal analysis, Data curation. **Chenjie Lou:** Formal analysis, Data curation. **Shuaika Liang:** Formal analysis, Data curation. **Wei Xia:** Investigation, Formal analysis. **Rui Wang:** Writing – original draft, Resources, Funding acquisition. **Longfei Li:** Data curation. **Chengyu Fu:** Data curation. **Mingxue Tang:** Resources, Investigation, Formal analysis, Data curation. **Rong Xiang:** Writing – review & editing, Funding acquisition. **Wei Wang:** Writing – review & editing, Formal analysis. **Yichun Xu:** Writing – original draft, Formal analysis, Data curation. **Hongfa Xiang:** Writing – review & editing, Supervision, Resources, Funding acquisition, Conceptualization. **Xuyong Feng:** Writing – review & editing, Supervision, Investigation, Funding acquisition, Conceptualization.

Declaration of competing interest

The authors declare that they have no known competing financial interests or personal relationships that could have appeared to influence the work reported in this paper.

Acknowledgments

This study was supported by the National Natural Science Foundation of China (Nos. U2330101, 52072105), the Major Science and Technology Projects in Anhui Province (Nos. 202203a05020032 and 2022e03020004), Innovation R&D Program of Anhui Province (No. 202423i08050026), Ministry of Science and Technology of China (No. 2023YFE0101300) and Zhejiang Province (No. 2022R01001), XXX-Project (No. 2020-XXXX-XX-246–00) and the Fundamental Research Funds for the Central Universities (No. JZ2024HGTG0292).

Supplementary materials

Supplementary material associated with this article can be found, in the online version, at doi:10.1016/j.cclet.2025.111558.

References

[1] S. Xin, X. Zhang, L. Wang, et al., Sci. China Chem. 67 (2024) 13–42.
[2] X. Yao, S. Chen, C. Wang, et al., Adv. Energy Mater. 14 (2023) 2303422.
[3] M.J. Wang, E. Carmona, A. Gupta, P. Albertus, J. Sakamoto, Nat. Commun. 11 (2020) 5201.
[4] Y. Li, X. Chen, A. Dolocan, et al., J. Am. Chem. Soc. 140 (2018) 6448–6455.
[5] X. Wang, Y. Chang, Y. Zhang, et al., Chin. Chem. Lett. 37 (2026) 110626.
[6] Y. Feng, L. Yang, Z. Yan, et al., Energy Storage Mater. 63 (2023) 103053.
[7] N. Kamaya, K. Homma, Y. Yamakawa, et al., Nat. Mater. 10 (2011) 682–686.
[8] F. Du, X. Ren, J. Yang, J. Liu, W. Zhang, J. Phys. Chem. C 118 (2014) 10590–10595.
[9] F. Han, Y. Zhu, X. He, Y. Mo, C. Wang, Adv. Energy Mater. 6 (2016) 1501590.
[10] J. Liang, X. Li, S. Wang, et al., J. Am. Chem. Soc. 142 (2020) 7012–7022.
[11] X. Li, J. Liang, J. Luo, et al., Energy Environ. Sci. 12 (2019) 2665–2671.
[12] Z. Jiang, C. Liu, J. Yang, et al., Chin. Chem. Lett. 36 (2025) 109741.
[13] F. Tu, Z. Zhao, X. Zhang, et al., ACS Sustain. Chem. Eng. 10 (2022) 15365–15371.
[14] T. Thompson, J. Wolfenstine, J.L. Allen, et al., J. Mater. Chem. A 2 (2014) 13431–13436.
[15] Y. Zeng, B. Ouyang, J. Liu, et al., Science 378 (2022) 1320–1324.
[16] Q. Wang, Z. Jiang, C. Yu, L. Li, G. Li, Chin. Chem. Lett. 36 (2025) 110006.
[17] D. Zuo, L. Yang, Z. Zou, et al., Adv. Energy Mater. 13 (2023) 2301540.
[18] L. Hu, J. Wang, K. Wang, et al., Nat. Commun. 14 (2023) 3807.
[19] K. Wang, Q. Ren, Z. Gu, et al., Nat. Commun. 12 (2021) 4410.
[20] H. Kwak, D. Han, J. Lyoo, et al., Adv. Energy Mater. 11 (2021) 2003190.
[21] S. Zhang, F. Zhao, L.Y. Chang, et al., J. Am. Chem. Soc. 146 (2024) 2977–2985.
[22] S. Chen, C. Yu, S. Chen, et al., Chin. Chem. Lett. 33 (2022) 4635–4639.
[23] Y. Ye, Z. Gu, J. Geng, et al., Nano Lett. 25 (2025) 3747–3755.
[24] N. Tanibata, S. Takimoto, K. Nakano, et al., ACS Mater. Lett. 2 (2020) 880–886.
[25] N. Flores-González, N. Minafra, G. Dewald, et al., ACS Mater. Lett. 3 (2021) 652–657.
[26] W. Weppner, R.A. Huggins, J. Electrochem. Soc. 124 (1977) 35–38.
[27] S. Zhang, Y. Xu, H. Wu, et al., Angew. Chem. Int. Ed. (2024) e202401373.
[28] L. Xu, X. Hu, S. Zhou, et al., Chin. Chem. Lett. 35 (2024) 109103.
[29] Y. Wang, W.D. Richards, S.P. Ong, et al., Nat. Mater. 14 (2015) 1026–1031.
[30] Y. Li, S. Song, H. Kim, et al., Science 381 (2023) 50–53.
[31] Y. Kato, S. Hori, T. Saito, et al., Nat. Energy 1 (2016) 16030.
[32] W.D. Richards, Y. Wang, L.J. Miara, et al., Energy Environ. Sci. 9 (2016) 3272–3278.
[33] X. Feng, P.H. Chien, S. Patel, et al., Chem. Mater. 32 (2020) 3036–3042.
[34] Y.C. Yin, J.T. Yang, J.D. Luo, et al., Nature 616 (2023) 77–83.
[35] C. Fu, Y. Li, W. Xu, et al., Nat. Commun. 15 (2024) 4315.
[36] J. Zhang, C. Lou, L. Dong, et al., Small Struct. 5 (2024) 2300565.
[37] X. Wang, R. Xiao, H. Li, L. Chen, Phys. Chem. Chem. Phys. 18 (2016) 21269–21277.
[38] X. Feng, P.H. Chien, Y. Wang, et al., Energy Storage Mater. 30 (2020) 67–73.
[39] S. Zhang, F. Zhao, L.Y. Chang, et al., J. Am. Chem. Soc. 146 (2024) 2977–2985.
[40] S. Zhang, F. Zhao, J. Chen, et al., Nat. Commun. 14 (2023) 3780.
[41] Y. Tanaka, K. Ueno, K. Mizuno, et al., Angew. Chem. Int. Ed. (2023) e202217581.
[42] Z. Liu, S. Ma, J. Liu, et al., ACS Energy Lett. 6 (2021) 298–304.
[43] T. Dai, S. Wu, Y. Lu, et al., Nat. Energy 8 (2023) 1221–1228.
[44] Y. Tan, J. Gatts, C. Fu, et al., Small 21 (2025) 2504677.
[45] Y. Wang, W.D. Richards, S.P. Ong, et al., Nat. Mater. 14 (2015) 1026–1031.
[46] Y. Gao, J. Liu, C. Lou, et al., Chin. Chem. Lett. 34 (2023) 108268.
[47] Y. Shi, W. Zhang, L. Xu, et al., Chin. Chem. Lett. 37 (2026) 111077.
[48] G. Yang, Z. Hao, C. Fang, et al., Chin. Chem. Lett. 36 (2025) 111185.
[49] F. Han, A.S. Westover, J. Yue, et al., Nat. Energy 4 (2019) 187–196.
[50] X. Fan, X. Ji, F. Han, et al., Sci. Adv. 4 (2018) eaau9245.
[51] X. Feng, P. Chien, Z. Zhu, et al., Adv. Funct. Mater. 29 (2019) 1807951.
[52] D. Wang, G. Zhong, W.K. Pang, et al., Chem. Mater. 27 (2015) 6650–6659.
[53] C.L. Farrow, P. Juhas, J.W. Liu, et al., J. Phys.: Condens. Matter 19 (2007) 335219.
[54] Q. Wang, X. Ma, Q. Liu, D. Sun, X. Zhou, J. Alloy. Compd. 969 (2023) 172479.
[55] Y. Ye, J. Geng, D. Zuo, et al., ACS Nano 18 (2024) 18368–18378.
[56] H. Pan, M. Zhang, Z. Cheng, et al., Sci. Adv. 8 (2022) eabn4372.
[57] M.A. Kraft, S. Ohno, T. Zinkevich, et al., J. Am. Chem. Soc. 140 (2018) 16330–16339.

[58] X. Li, J. Liang, X. Yang, et al., Energy Environ. Sci. 13 (2020) 1429–1461.
[59] H. Kwak, S. Wang, J. Park, et al., ACS Energy Lett. 7 (2022) 1776–1805.
[60] J. Lau, R.H. DeBlock, D.M. Butts, et al., Adv. Energy Mater. 8 (2018) 1800933.
[61] L. Xu, J. Li, W. Deng, et al., Adv. Energy Mater. 11 (2021) 2000648.
[62] C. Wang, J.T. Kim, C. Wang, X. Sun, Adv. Mater. 35 (2023) 2209074.
[63] K.N. Gao, F. Bai, Z. Sun, T. Zhang, Energy Storage Mater. 70 (2024) 103444.
[64] A. Manthiram, X. Yu, S. Wang, Nat. Rev. Mater. 2 (2017) 16103.
[65] K. Tuo, C. Sun, S. Liu, Energy Rev. 6 (2023) 17.
[66] P. Lu, D. Wu, L. Chen, H. Li, F. Wu, Electrochem. Energy Rev. 5 (2022) 3.
[67] Y.G. Lee, S. Fujiki, C. Jung, et al., Nat. Energy 5 (2020) 299–308.